Geophysical Research Letters

RESEARCH LETTER
10.1029/2022GL099077

Key Points:

- Seismicity analysis suggests that both external and internal forcing drive deformation in the Armutlu Peninsula
- Temporal correlation between a slow-slip transient and seismic *b*-value highlights interactions between aseismic and seismic deformation
- Slow-slip transients modulate the frequency-magnitude and spatiotemporal earthquake distribution

Supporting Information:

Supporting Information may be found in the online version of this article.

Correspondence to:

G. M. Bocchini,
gian.bocchini@rub.de

Citation:

Bocchini, G. M., Martínez-Garzón, P., Verdecchia, A., Harrington, R. M., Bohnhoff, M., Turkmen, T., & Nurlu, M. (2022). Direct evidence of a slow-slip transient modulating the spatiotemporal and frequency-magnitude earthquake distribution: Insights from the Armutlu Peninsula, northwestern Turkey. *Geophysical Research Letters*, *49*, e2022GL099077. https://doi.org/10.1029/2022GL099077

Received 12 APR 2022
Accepted 5 SEP 2022

Direct Evidence of a Slow-Slip Transient Modulating the Spatiotemporal and Frequency-Magnitude Earthquake Distribution: Insights From the Armutlu Peninsula, Northwestern Turkey

G. M. Bocchini[1], P. Martínez-Garzón[2], A. Verdecchia[1], R. M. Harrington[1], M. Bohnhoff[2,3], T. Turkmen[4], and M. Nurlu[4]

[1]Faculty of Geosciences, Institute of Geology, Mineralogy and Geophysics, Ruhr University Bochum, Bochum, Germany, [2]Helmholtz Centre Potsdam GFZ German Research Centre for Geosciences, Geomechanics and Scientific Drilling, Potsdam, Germany, [3]Free University of Berlin, Institute of Geological Sciences, Berlin, Germany, [4]AFAD Turkish Disaster Management Presidency, Ankara, Turkey

Abstract Earthquakes and slow-slip events interact, however, detailed studies investigating their interplay are still limited. We generate the highest resolution microseismicity catalog to date for the northern Armutlu Peninsula in a ∼1-year period to perform a detailed seismicity distribution analysis and correlate the results with a local, geodetically observed slow-slip transient within the same period. Seismicity shows a transition of cluster-type behavior from swarm-like to burst-like, accompanied by an increasing relative proportion of clustered (non-Poissonian) relative to background (Poissonian) seismicity and gradually decreasing *b*-value as the geodetically observed slow-slip transient ends. The observed slow-slip transient decay correlates with gradually increasing effective-stress-drop values. The observed correlation between the *b*-value and geodetic transient highlights the influence of aseismic deformation on seismic deformation and the impact of slow-slip transients on local seismic hazard.

Plain Language Summary Seismic and aseismic slip on faults can change the stress state in the crust and affect the recurrence time of earthquakes. Observations of how earthquakes and aseismic fault slip influence each other are limited because of the dearth of synchronous high-resolution seismological and geodetic data. Here we use high-resolution earthquake data in the northern Armutlu Peninsula along the Marmara seismic gap of the North Anatolian Fault (Turkey) to correlate the earthquake distribution with a local slow-slip transient that occurred in the same period. We find that the slow-slip transient modulates the spatiotemporal and frequency-magnitude evolution of earthquakes, which highlights the influence of slow fault creep on fast fault slip. Our study demonstrates the importance of considering slow-slip transients for seismic hazard assessment.

1. Introduction

The underlying physical mechanisms driving seismicity control its spatiotemporal evolution. Classic "mainshock-aftershock" sequences are largely driven by earthquake-earthquake interaction via Coulomb stress transfer (King et al., 1994) and follow an Omori law decay. Conversely, swarms have no obvious mainshock and commonly exhibit a complex spatiotemporal evolution. They are often associated with external forcing by migrating fluids and/or aseismic slip, which likely operate on different time scales (De Barros et al., 2020; Hainzl & Ogata, 2005; Lohman & McGuire, 2007; Ross et al., 2020). The physical conditions favoring swarm over mainshock-aftershock sequences are still poorly understood and may relate to the stress state and frictional properties of faults. In fact, temporal variation of *b*-values during swarms (Hainzl & Fischer, 2002; Yoshida et al., 2017) and the transition from swarm to mainshock-aftershock sequences (Bachura et al., 2021) have been interpreted to reflect stress and/or frictional strength variations. The inverse correlation between *b*-value and differential stress suggests that lower *b*-values reflect local stress concentrations favoring the growth of larger earthquakes (Goebel et al., 2012; Scholz, 1968; Schorlemmer et al., 2005).

Documented observations of spatiotemporal seismicity variations have highlighted interactions between seismic and aseismic fault slip in a variety of tectonic settings (Cruz-Atienza et al., 2021; Mouslopoulou et al., 2020;

Tormann et al., 2013). Slow-slip transients often precede large magnitude earthquakes (Cruz-Atienza et al., 2021; Uchida et al., 2016) and large earthquakes can trigger slow-slip transients via static and/or dynamic stress perturbations (Cruz-Atienza et al., 2021; Koulali et al., 2017). Current detection thresholds of seismic signals are lower than those of aseismic signals, and the occurrence of slow-slip transients during seismic sequences is often indirectly inferred by seismological observations (De Barros et al., 2020; Uchida & Bürgmann, 2019). The scarcity of synchronous high-resolution seismological and geodetic data therefore hinders widespread analysis of spatiotemporal interactions between seismic and aseismic deformation.

The northern Armutlu Peninsula in the eastern Sea of Marmara, northwestern Turkey, offers a natural laboratory to study the underlying processes that govern the spatiotemporal seismicity evolution. The region hosts high-seismicity rates with strong spatiotemporally correlated activity (Martínez-Garzón, Ben-Zion, et al., 2019), slow-slip transients (Aslan et al., 2019; Durand et al., 2022; Martínez-Garzón, Bohnhoff, et al., 2019, 2021), and intense hydrothermal activity (Eisenlohr, 1997). It also hosts the only onshore segment of the North Anatolian Fault (i.e., Çınarcık fault) along the Marmara seismic gap (Figure 1a) (Bohnhoff et al., 2013; Parsons, 2004), which was densely instrumented in 2019–2020 during the SMARTnet seismic experiment (Figures 1a and 1b) (Martínez-Garzón et al., 2021, Martínez-Garzón, Bohnhoff, et al., 2022). A period of increased seismicity started at the end of November 2018 and includes a M_w 4.1 on 30 November 2018 and a M_w 4.5 on 20 December 2018, both activating an onshore local normal fault (Figures 1a–1c, Martínez-Garzón et al., 2021).

In this study, we generate an enhanced, high-resolution microseismicity catalog from 25 January 2019 to 7 February 2020 to analyze the spatiotemporal earthquake distribution in the northern Armutlu peninsula that incorporates data from the SMARTnet experiment. We examine in detail the seismicity contemporaneous to a nearby aseismic strain transient that initiated on 20 December 2018, the same day as the M_w 4.5 earthquake (Martínez-Garzón et al., 2021). The strain signal duration of ∼250 days (Figure 1c) exceeded the typical few-day duration of afterslip signals of $M < 5$ events (Hawthorne et al., 2016), leading to the interpretation as a slow-slip transient (Martínez-Garzón et al., 2021).

In the following, we discuss the physical conditions underlying swarm and mainshock-aftershock sequences and describe the relations between aseismic and seismic-slip episodes, along with their seismic hazard implications.

2. Data and Methods

We conduct a matched-filter search using the software EQcorrscan (Chamberlain et al., 2018) to create a high-resolution catalog of the study region. We construct templates using 807 events and phase-picks from the relocated catalog of Martínez-Garzón et al. (2021) considering waveforms from land and borehole stations (Figure 1a, Text S1 in Supporting Information S1). We compute detections between 25 January 2019 to 7 February 2020 by cross-correlating P- and S-wave signal windows on vertical and horizontal channels, respectively. We locate events with five or more cross-correlation derived phase-picks in NonLinLoc (Lomax et al., 2000) using a local 1D velocity model (Bulut et al., 2009). We estimate relative magnitudes based on amplitude differences using EQcorrscan routines (Chamberlain et al., 2018) to create a final list of both template events and new detections. Text S1 in Supporting Information S1 details the matched-filter detection procedure. We then improve relative locations in HypoDD (Waldhauser, 2001) using both P- and S-phase cross-correlation and catalog differential arrival times to provide a detailed image of activated seismic structures and their relative geometries. Text S2 in Supporting Information S1 details the relocation method.

Next, we analyze the temporal b-value evolution to investigate the seismicity frequency-magnitude-distribution (FMD) variation in space and time. To avoid b-value estimation bias due to changes in the magnitude of completeness (M_c) (Hainzl, 2016), we jointly estimate both parameters using 50% overlapping windows of 600 events and compare their trends. We calculate b-value and M_c using the maximum likelihood method (Utsu, 1965) and goodness-of-fit test (Wiemer & Wyss, 2000), respectively. We report mean values of 1,000 bootstrap runs and 68% confidence intervals.

We then estimate effective stress drop ($\Delta\sigma_{eff}$) values of individual seismic sequences to investigate possible aseismic deformation along fault segments (Fischer & Hainzl, 2017). The $\Delta\sigma_{eff}$ is estimated with equations similar to the stress drop for a single circular crack (Madariaga & Ruiz, 2016), where the total rupture area of the cluster is analogous to the rupture area of the crack (Fischer & Hainzl, 2017). Similar to the single crack, an increase in rupture area relative to slip for a given seismic moment corresponds to a lower stress-drop value. The release of

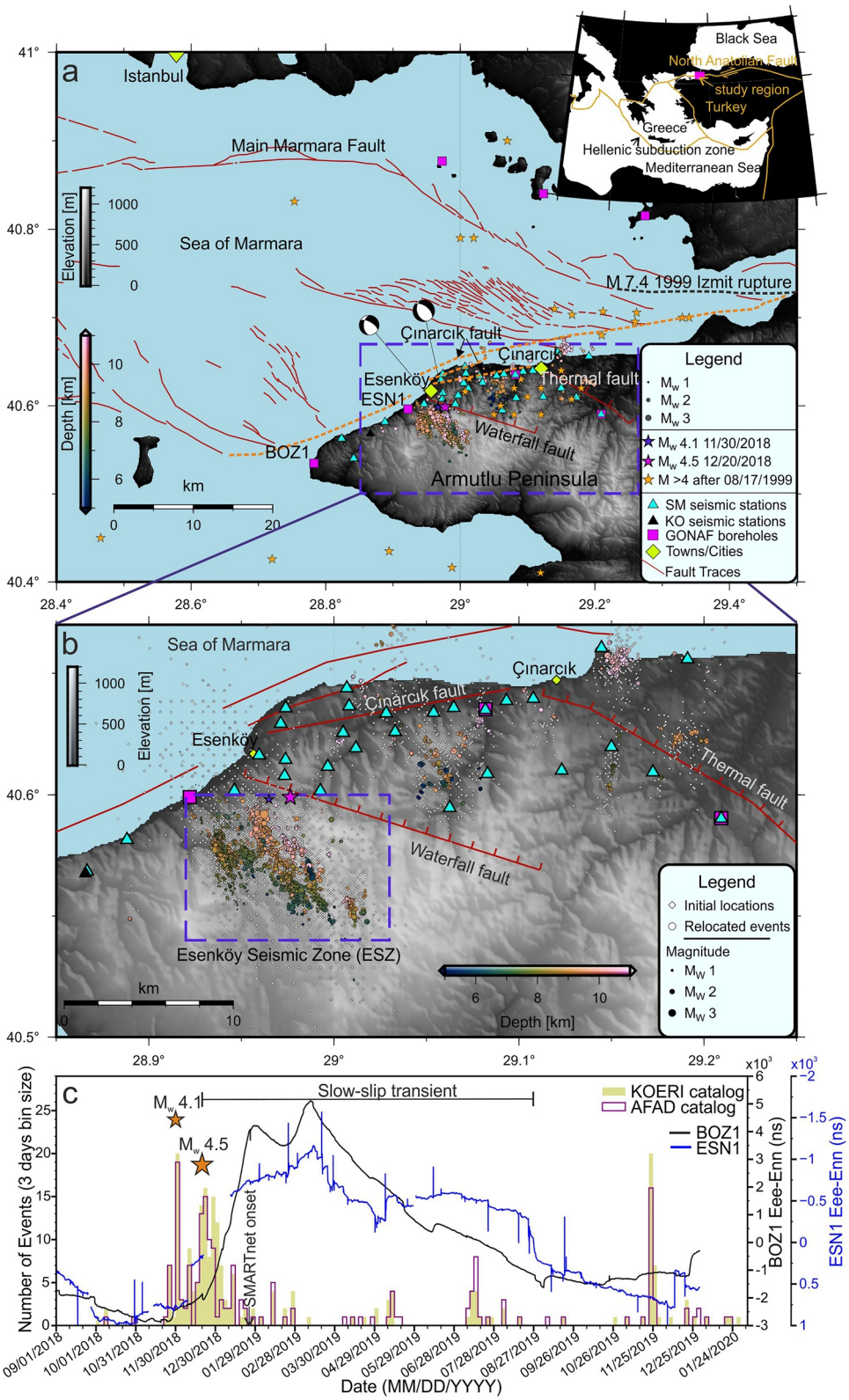
a
Istanbul
Main Marmara Fault
Sea of Marmara
M 7.4 1999 Izmit rupture
Çınarcık fault
Çınarcık
Esenköy
ESN1
Thermal fault
Waterfall fault
BOZ1
Armutlu Peninsula
Black Sea
North Anatolian Fault
study region
Turkey
Greece
Hellenic subduction zone
Mediterranean Sea
Elevation [m]
Depth [km]
km
Legend
Mw 1
Mw 2
Mw 3
Mw 4.1 11/30/2018
Mw 4.5 12/20/2018
M >4 after 08/17/1999
SM seismic stations
KO seismic stations
GONAF boreholes
Towns/Cities
Fault Traces
b
Esenköy Seismic Zone (ESZ)
Initial locations
Relocated events
Magnitude
Depth [km]
c
Slow-slip transient
KOERI catalog
AFAD catalog
BOZ1
ESN1
SMARTnet onset
Number of Events (3 days bin size)
BOZ1 Eee-Enn (ns)
ESN1 Eee-Enn (ns)
Date (MM/DD/YYYY)

Figure 1.

stress by aseismic deformation commonly results in lower $\Delta\sigma_{eff}$ compared to the typical range static stress drop values for individual events (0.1–100 MPa) (Fischer & Hainzl, 2017).

Furthermore, we quantify the seismicity dynamics and event interaction using a nearest-neighbor cluster analysis (Zaliapin & Ben-Zion, 2013a, 2013b; Zaliapin et al., 2008). The nearest-neighbor cluster analysis combines inter-event distances and times rescaled by the magnitude-frequency distribution to individuate clusters of linked events. The largest magnitude event in a cluster is called "mainshock", and remaining events occurring before and after the mainshock are termed "foreshocks" and "aftershocks", respectively. The term "singles" denotes isolated events that lack links with other events. The sum of aftershocks and foreshocks represents clustered (non-Poissonian) seismicity, while the sum of mainshocks and singles represents background (Poissonan) seismicity. We apply a 1D Gaussian mixture model (Figure S1 in Supporting Information S1, Martínez-Garzón et al., 2018; Zaliapin & Ben-Zion, 2016) to separate background from clustered seismicity. For each cluster, we calculate the average leaf depth (d_m), namely the average topological distance from the cluster leaves (earthquakes with no offspring) to the root (first earthquake in the cluster) (Zaliapin & Ben-Zion, 2013a, 2013b). Larger d_m are typical of swarm-like sequences, while smaller d_m are typical of burst-like (mainshock-aftershocks) sequences. Text S3 in Supporting Information S1 details the nearest-neighbor method.

Finally, we identify families of highly similar events using waveform-based clustering using *Clusty* (Petersen et al., 2021). We cross-correlate P- and S-wave phases on vertical and horizontal channels, respectively, for all event pairs within 10 km hypocentral distance. Text S4 in Supporting Information S1 details the waveform-based clustering approach.

3. Results

3.1. Enhanced and Relocated Microseismicity Catalogs

The initial enhanced matched-filter catalog contains 7,677 events and displays a M_c 0.8 (Figure 1b). It has average vertical location errors of 2.4 ± 1.2 km and horizontal semi-minor and semi-major axes error ellipses of 1.8 ± 1.5 and 5.2 ± 3.0 km, respectively, within the 68% confidence interval. We successfully relocate 4,182 events with relative horizontal and vertical location errors of 100 and 40 m, respectively, estimated from bootstrap resampling of 1,000 trials using the 68% confidence interval. The relocated catalog illuminates the complex tectonics of the northern Armutlu Peninsula in unprecedented detail. The seismicity shows strong spatial clustering of 3,381/4,128 events (82%) within a narrow ~60 km^2 region (Figures 1b and 2) that release 86% of the total seismic moment (M_0) of the relocated catalog. We refer to the most seismically active region during our study period as the "Esenköy Seismic Zone" (ESZ) (Figures 1b and 2). We note that the cluster analysis employs the relocated catalog, given the highly similar cumulative M_0 and temporal distribution of events with respect to the initial catalog (Figure 3a).

3.2. Spatiotemporal Evolution, *b*-Values and Effective Stress Drop of Seismicity Within the ESZ

The seismicity within the ESZ exhibits strong temporal clustering that highlights four distinct sequences: (a) Sequence 1 from 25 January 2019 to 28 February 2019 (contemporaneous onset with SMARTnet operation), (b) Sequence 2 from 6 May 2019 to 16 May 2019, (c) Sequence 3 from 9 July 2019 to 19 July 2019, and (d) Sequence 4 from 22 November 2019 to 29 November 2019 (Figures 2 and 3a). The seismic activity within sequences exhibits negligible spatial overlap (except for partial overlap of Sequences 1–2), suggesting the activation of different faults and/or segments. Sequences exhibit distinct temporal distribution of event frequencies and magnitudes (Figure S2 in Supporting Information S1).

Sequence 1 shows the widest spatial extent and delineates a NW-SE striking normal fault dipping ~60° toward NE at depths of 6–11 km (Figure 2). The seismicity distribution in map-view shows NW-SE or NNW-SSE elongated

Figure 1. (a) Armutlu Peninsula and eastern Sea of Marmara seismotectonic map. Solid brown lines represent fault traces (Armijo et al., 2002; Kinscher et al., 2013). Dashed orange line indicates Çınarcık segment, dashed black line indicates offshore extension of the M 7.4 17 August 1999 Izmit rupture (Barka et al., 2002). Orange stars represent epicenters of $M > 4$ earthquakes following the Izmit earthquake (KOERI, 1971). Focal mechanisms of the 30 November 2018 M_w 4.1 and 20 December 2018 M_w 4.5 earthquakes (beach-balls) and relocated events (circles) are from Martínez-Garzón et al. (2021). SM, SMARTnet; KO, KOERI. (b) enhanced seismicity catalog 25 January 2019 to 7 February 2020 from this study. Dashed purple rectangle delineates the Esenköy Seismic Zone. (c) temporal seismicity distribution from KOERI (KOERI, 1971) and AFAD (AFAD, 2022) catalogs (1 September 2018 to 7 February 2020, latitude 40.44-40.64 and longitude 28.90-29.04) and differential component of the strain signal recorded from strainmeters BOZ1 and ESN1.

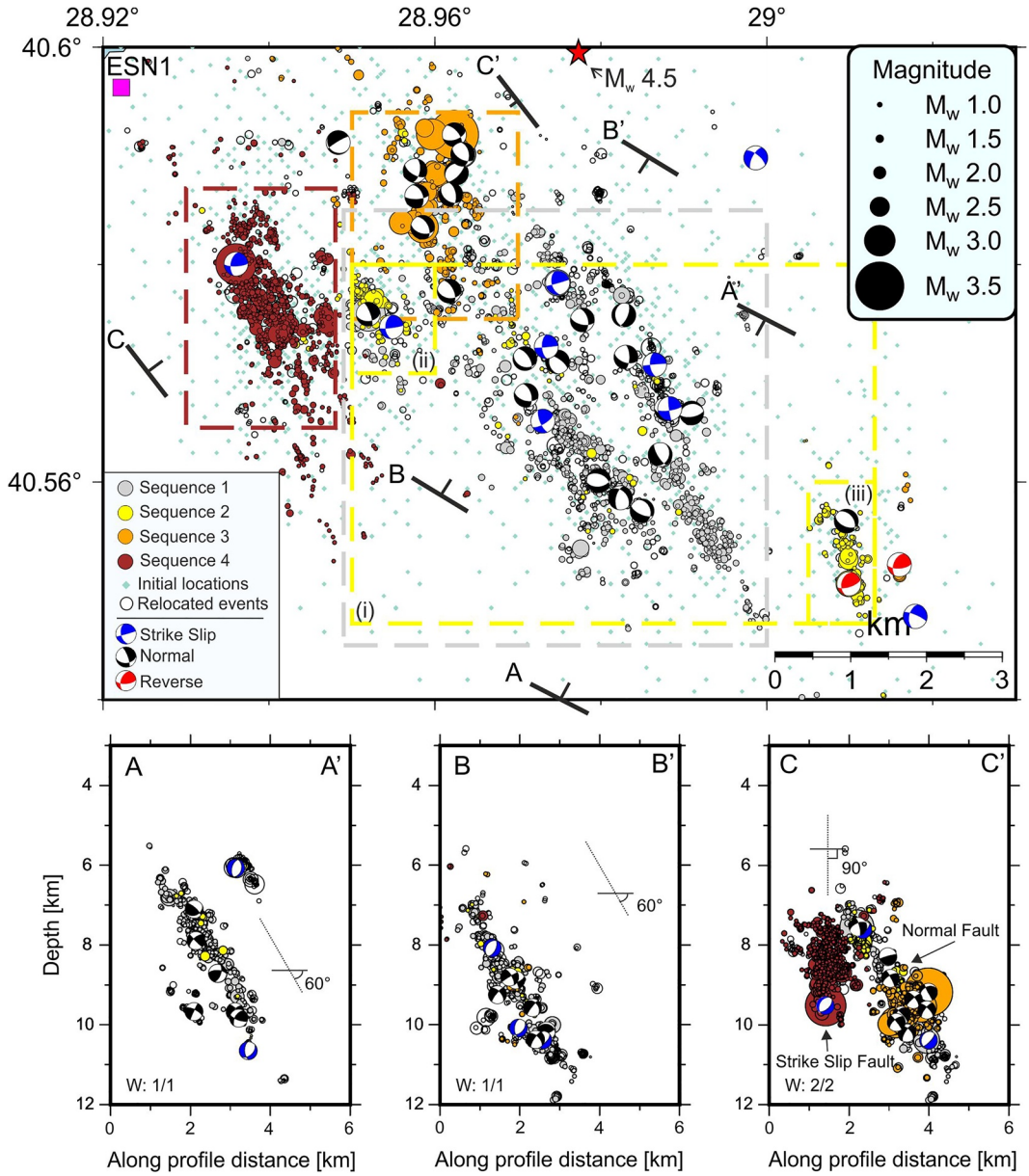

Figure 2. Esenköy Seismic Zone seismicity. Colored circles denote events within four seismic sequences. Dashed boxes include initial event selection for effective stress drop estimates (Section 3.2). We consider two scenarios for Sequence 2: (1) single sequence (i); (2) two sequences, including a northern (ii) and a southern cluster (iii). *W* is width (km) of cross-sections (left/right). We include high quality (RMS ≤ 0.6 and ≥10 polarity readings) focal mechanisms (Martínez-Garzón et al., 2021) of background events (see text).

clusters separated by regions with a dearth of seismicity. It exhibits elevated *b*-values varying between ~1.4–1.6, indicating a larger proportion of smaller-magnitude events (Figure 3b). The $\Delta\sigma_{eff}$ of ~0.02 MPa (Figure 3a) suggests a low cumulative M_0 release relative to total activated area.

Sequence 2 activates two distinct regions to the NW (hereafter northern cluster, *ii* in Figure 2) and SE (hereafter southern cluster, *iii* in Figure 2) of the normal fault active during Sequence 1. Cluster *ii* spatially overlaps with seismic activity during Sequence 1, while Cluster *iii* is separated from it by a ~1 km gap (Figure 2). In addition, a minor number of events occur over the same structure active in Sequence 1. Sequence 2 exhibits *b*-values of ~1.4 (Figure 3b) and $\Delta\sigma_{eff}$ of ~0.01 MPa, similar to values in Sequence 1. However, the ~5 km between Clusters *ii* and *iii* suggests they may not be related to the same underlying process. Thus, we also calculate the $\Delta\sigma_{eff}$ of Cluster *ii* and *iii* separately, obtaining values of ~1 and ~0.35 MPa, respectively (Figure 3a).

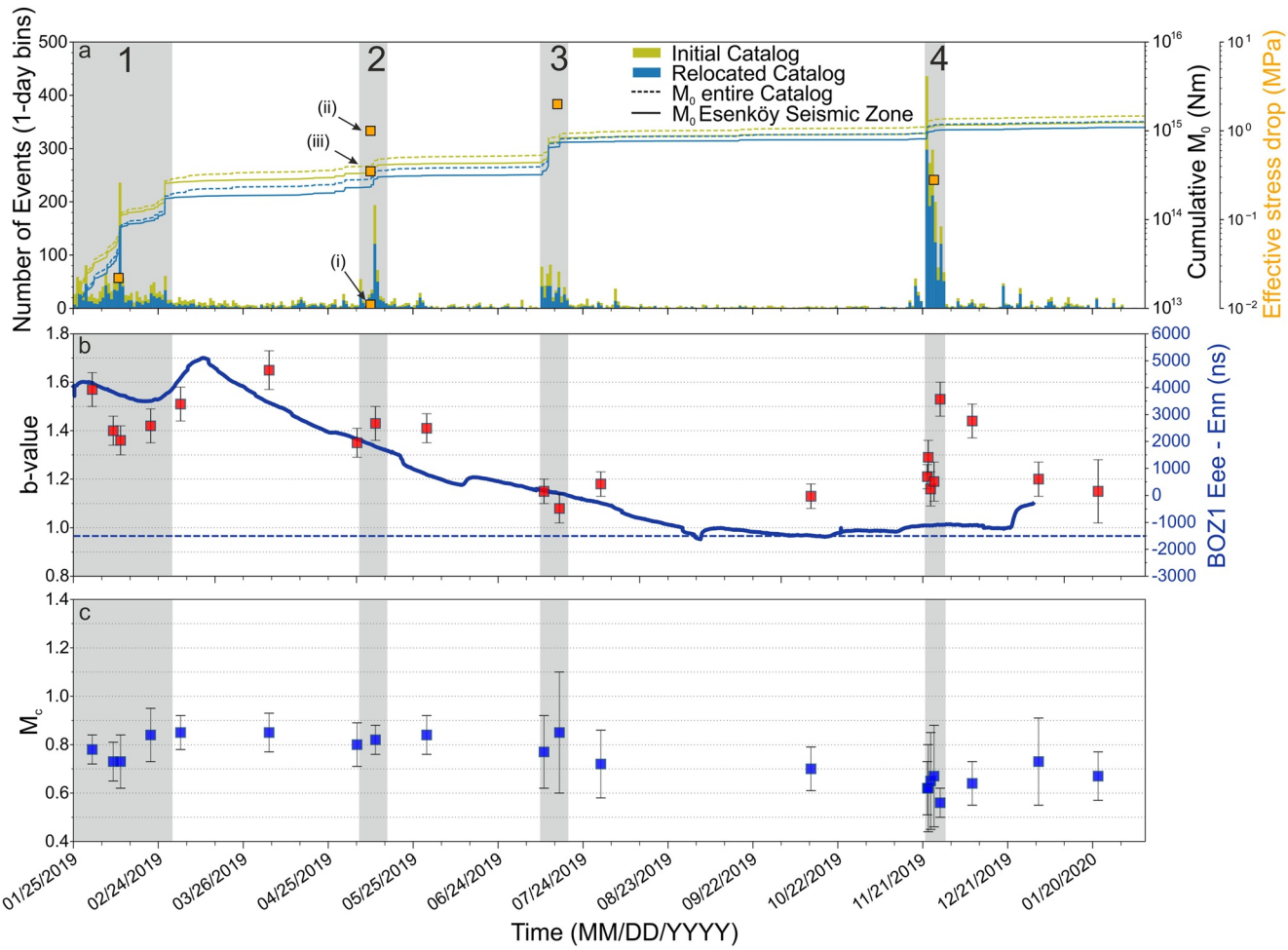

Figure 3. Spatiotemporal seismicity distribution. (a) daily event number and cumulative M_0 versus time. Orange squares report $\Delta\sigma_{eff}$ estimates of individual sequences. For Sequence 2: (i) entire cluster, (ii) northern cluster; (iii) southern cluster (Figure 2). (b) *b*-value evolution. Continuous blue line shows differential strain component at strainmeter BOZ1 (Figure 1); horizontal dashed blue line indicates approximate strain level before 20 December 2018. (c) temporal evolution of completeness magnitude (M_c). Vertical bars (b–c) denote 68% confidence interval. We obtain *b*-values and M_c from events in the initial enhanced catalog. Gray shaded areas (a–c) denote temporal intervals of the four sequences.

Sequence 3 concentrates within a narrow area at 9–10 km depth and hosts the largest event in the catalog, a M_w 3.5 on 11 July 2019 (Figure 2). Despite its lower event numbers relative to the other sequences, especially in January, February and November, it releases substantially larger cumulative M_0 (Figure 3a). Seismicity concentrates along the NW continuation of the normal fault activated during Sequence 1 and partly in May and has a less clear geometry at depth. The *b*-value of ∼1.1 is the smallest among the sequences, while the $\Delta\sigma_{eff}$, ∼2 MPa is the largest (Figure 3a).

Sequence 4 occurs in the westernmost part of the ESZ and activates a vertical strike-slip fault at 7.5–10 km depth (Figure 2). We observe *b*-values of ∼1.1–1.2 at the beginning of the sequence that rapidly increase to ∼1.5 (Figure 3b). The sequence exhibits $\Delta\sigma_{eff}$ of ∼0.28 MPa (Figure 3a).

Notably, the temporal *b*-value variations correlate positively with the slow-slip transient observed in Martínez-Garzón et al. (2021) during the same period. The high *b*-value of ∼1.4–1.6 during the period of high-strain level decreases with time approaching ∼1.1, when the transient strain signal reaches a plateau and approaches pre-transient levels, suggesting recovery from a perturbed stress state (pre-20 December 2018) (Figure 3b). The temporal *b*-value variations correlate poorly with M_c variations that show only minor oscillations around the average value of 0.8 (Figures 3b and 3c). We observe a similar *b*-value evolution and correlation with the slow-slip transient, even when using events from the relocated catalog and different event windows (Figures S3 and S4 in Supporting Information S1). The systematically lower M_c from mid-end of July 2019 onward is explained by

the deployment of five additional seismometers in July 2019 (Figure 3c, Text S1 in Supporting Information S1, Martínez-Garzón et al., 2021).

3.3. Nearest-Neighbor Cluster Analysis

The nearest-neighbor approach estimates that 37% and 63% of events represent background and clustered seismicity, respectively. Figure 4a shows the distribution of rescaled times and distances from our catalog. The gradual decrease in background seismicity from January to the beginning of August correlates with the decrease in the strain level at nearby strainmeters (Figure S5 in Supporting Information S1).

Comparing d_m with the size of clusters with ≥10 events reveals two distinct cluster groups (Figure 4b). In the first group, d_m increases quickly with the cluster size, which is typical of swarm-like clusters; in the second group, d_m gently increases with the cluster size, which is typical of burst-like clusters (Figure 4b). Based on the trend observed in Figure 4b, we define a d_m threshold of $\sim 4 \pm 0.5$ to separate swarm and burst-like activity. The two clusters containing the largest events in the catalog (M_w 3.5 on 11 July 2019 and M_w 3.3 on 22 November 2019) show clear burst-like behavior with $d_m < 3.5$ and cluster sizes of 93 and 276, respectively (Figure 4b).

We investigate the spatiotemporal evolution of the 32 clusters within the ESZ containing ≥10 events (Figures 4c, S6 in Supporting Information S1). Notably, the decrease of average d_m with time indicates a transition from swarm-like clusters in Sequences 1–2 toward burst-like clusters in Sequences 3–4 (Figure 4c). Moreover, the largest clusters in January-February and May display $d_m > 4.5$, while in July and November they display $d_m < 3.5$. Only one cluster has $d_m > 4.5$ within Sequence 3. The sequence in November initiates with a burst-like cluster of 276 events (the largest in the catalog) and it is followed by three swarm-like clusters ($d_m > 4.5$).

We analyze changes in the ratio of foreshocks, mainshocks, aftershocks, and singles between the four sequences to further investigate the underlying earthquake dynamics in the ESZ. We observe a gradual temporal decrease of the proportion of background seismicity with respect to the total number of events from 43.5% during the first sequence to 9.6% during the fourth sequence (Figure 4c). The decrease is mostly driven by a decrease in the number of singles, amounting to 32.4%, 13.7%, 8.2%, and 5.4% of the total number of events in Sequences 1–4 (Figure 4c). A change in the ratio between foreshocks and aftershocks accompanies an increase of clustered seismicity from Sequence 1 to 4. Generally, except for Sequence 2, where the foreshock-aftershock ratio is 1.40, it gradually decreases with time from 0.46 to 0.16, further supporting the overall transition from swarm- to burst-like cluster behavior (Figure 4c). Table S1 in Supporting Information S1 summarizes the event statistics discussed above.

3.4. Highly-Similar Event Clusters

We identify 29 highly similar event families or "repeaters" (without temporal constraints) from the relocated catalog. Repeater families are limited to 2–4 events and exhibit average inter-event times of a few hours, except for two families in February with average inter-event times exceeding a week (Figure S7 in Supporting Information S1). The ESZ hosts 23 repeater families, where 6, 5, 2, and 4, families occur in Sequence 1, 2, 3, and 4, respectively (Figure S8 in Supporting Information S1). Only two of the remaining six repeater families occur more than on week before or after the reported sequences, suggesting a correlation in the processes driving sequences and repeating earthquake activity.

4. Discussion

We focus the discussion on the description of Sequences 1–3 that occurred synchronously with the slow-slip transient. The two closest GONAF borehole strainmeters to the ESZ, ESN1 and BOZ1 (Figure 1a) recorded the transient strain signal, suggesting a proximal origin to the ESZ (Martínez-Garzón et al., 2021). Martínez-Garzón et al. (2021) proposed a location of the slow-slip transient on the shallower portion of the normal fault activated by the M_w 4.5 earthquake and Sequences 1–3 based on the available strainmeter data. We base the following interpretations on the occurrence of the slow-slip transient on the normal fault mentioned above, that, as we will discuss, is consistent with the spatiotemporal seismicity distribution.

Results from nearest-neighbor cluster analysis show a dominant, early swarm-like behavior contrasting the dominant burst-like behavior in July (Figure 4c). Where interpretations of swarm-like behavior commonly invoke

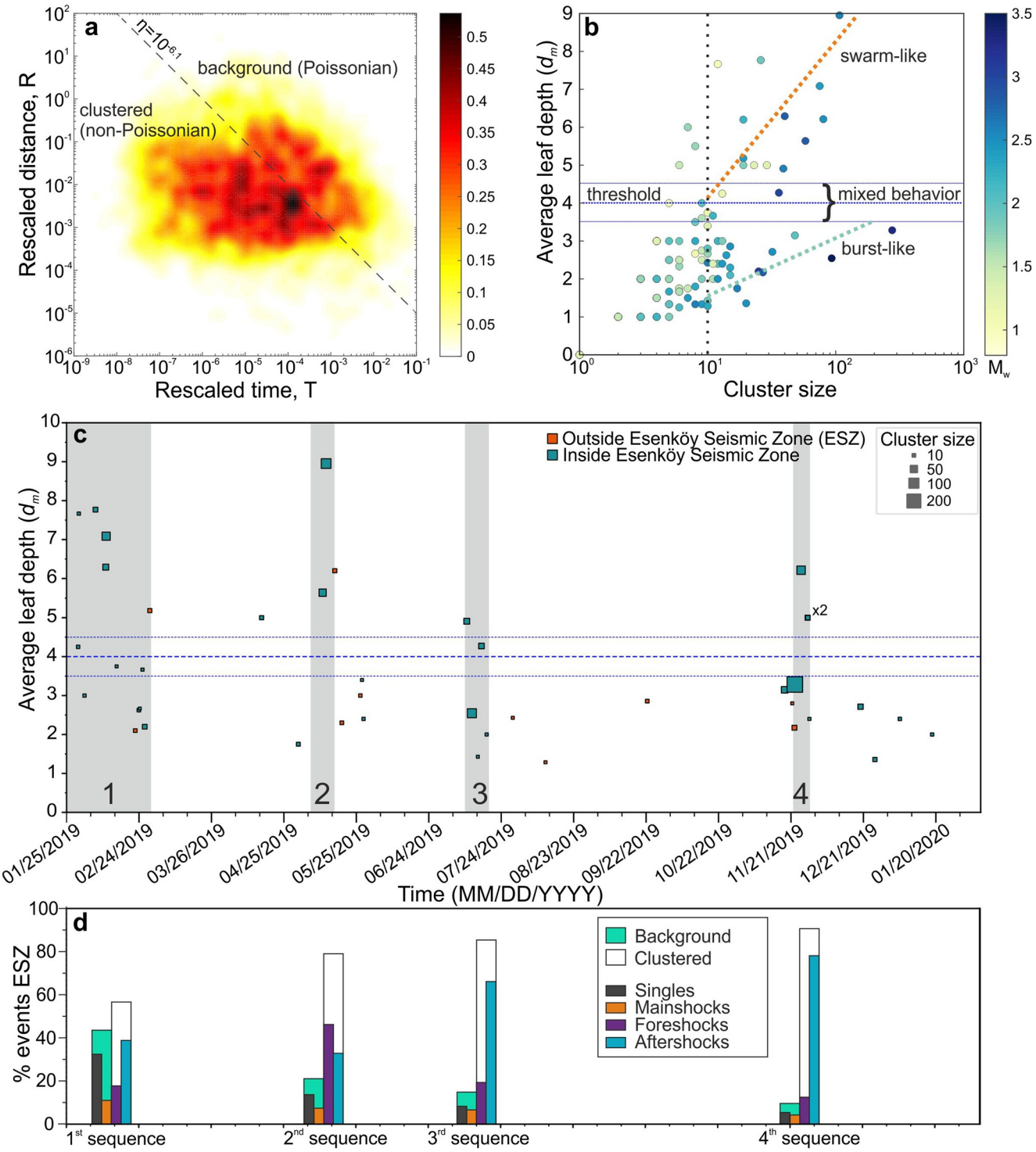

Figure 4. Nearest-neighbor cluster analysis results. (a) rescaled distance versus rescaled time. η, nearest-neighbor proximity. Colorbar represents the distribution of the density of event pairs. (b) average leaf depth (d_m) versus cluster size, with clusters colored according to mainshock magnitude. Dotted turquoise and orange lines delineate distribution of burst- and swarm-like clusters. (b-c) dashed horizontal lines denote threshold separating swarm- from burst-like clusters in this study (4 ± 0.5). (c) d_m versus time of clusters (squares) with ≥10 events. The gray shaded areas denote temporal intervals of Sequences 1–4. (d) percentage of singles, foreshocks, mainshocks, and aftershocks (thinner bars) and of background and clustered seismicity (thicker bars) relative to total events during individual sequences within the Esenköy Seismic Zone (ESZ).

external forcing by migrating fluids and/or aseismic slip, burst-like behavior is commonly interpreted to result from earthquake-earthquake interactions (De Barros et al., 2020; Hainzl et al., 2012; Hainzl & Fischer, 2002; Lohman & McGuire, 2007; Verdecchia et al., 2021). Thus, the transition of more swarm-like to burst-like cluster behavior suggests a decrease in the external forcing over Sequences 1–3, in agreement with the observed temporal decay of the concomitant local slow-slip transient that occurred on the same fault. To infer changes in external forcing, it is useful to consider a number of aspects, including: (a) the positive correlation between background seismicity and pore-pressure linked to hydraulic operations (Langenbruch et al., 2011; Zaliapin & Ben-Zion, 2016); (b) the acceleration of the rupture of isolated asperities (single events) at distances beyond those affected by earthquake-earthquake interactions during slow-slip propagation (Matsuzawa et al., 2004); and (c) the increase in the foreshock-aftershock ratio within seismic sequences driven by slow-slip transients (McGuire et al., 2005). Our results show: (a) decreasing proportion of background seismicity that correlates with the decrease of transient strain levels (Figure S5 in Supporting Information S1) and of the proportion of background to clustered seismicity; (b) a decay in number of single events; and (c) a decrease in the foreshock-aftershock ratio (Figure 4d), supporting the decrease in external forcing. The increased proportion of clustered seismicity over time could signify the build-up of stress over the region, which is consistent with temporal variations of the observed *b*-value (Figures 3b and 4d).

We observe a striking positive correlation between the *b*-value evolution and the recorded slow-slip transient (Figures 3b, S3, and S4 in Supporting Information S1). The inverse correlation between the *b*-value and differential stress (Scholz, 1968, 2015; Schorlemmer et al., 2005), in addition to the positive correlation between the *b*-value with pore pressure (Bachmann et al., 2012) and material heterogeneity (Goebel et al., 2017), suggests a link between the *b*-value and the shear stress and/or fault frictional strength (Tormann et al., 2014; Yoshida et al., 2017). Thus, our findings are consistent with a model where the earthquake FMD reflects changes in the stress regime and/or fault frictional strength modulated by aseismic deformation. Changes in the stress regime and/or fault frictional strength modulated by aseismic deformation may arise from different mechanisms. Tormann et al. (2013) observed a similar correlation between the seismic *b*-value and a shallow slow-slip transient along the Parkfield segment of the San Andreas Fault, proposing that earthquake FMD responds to variations in aseismic deformation rates that affect the fault stressing regime. They interpret slow-slip transients to release fault stresses that promote individual rupture, rather than coalescent rupture of embedded asperities that result in smaller magnitude earthquakes and higher *b*-value. Reduced on-fault aseismic deformation promotes shear stress increase, earthquake-earthquake interactions, and fracture coalescence that increase the probability of larger-magnitude earthquakes and reduce the *b*-value. However, slow-slip transients do not only reduce shear stress on the fault segment where they occur but may increase/decrease stresses on neighboring segments and/or faults (Obara & Kato, 2016). Segments where stress increases should exhibit a higher probability for larger-magnitude earthquakes and lower *b*-values and *vice versa*. An accurate location of the slow-slip transient would be needed to clarify the mechanisms by which the slow-slip transient modulates the earthquake FMD but is challenging with the available strainmeter data. Additionally, fault frictional strength may evolve over time due to changes in fault hydromechanical properties (Cappa et al., 2019), where slow-slip transients have been observed to modulate pore fluid pressures (Warren-Smith et al., 2019).

The proposed relation between the *b*-value and aseismic deformation is further supported by the observed variations of $\Delta\sigma_{\text{eff}}$ and the distribution of repeater families. The $\Delta\sigma_{\text{eff}}$ is comparatively low in January-February, implying notable aseismic stress release (Fischer & Hainzl, 2017) over the activated area, and increases toward July (Figure 3a). Repeater families are particularly abundant during Sequences 1–2 and decrease in July (Figures S7 and S8 in Supporting Information S1). De Barros et al. (2020), observed an increasing number of repeaters with short interevent times during seismic swarms driven by a combined effect of fluid diffusion and aseismic slip. In addition to external forcing by slow-slip, fluid migration along faults and pre-existing fractures could also promote vigorous seismic activity, especially in a region of intense hydrothermal activity (Eisenlohr, 1997). However, we observe no obvious seismicity migration patterns that are well described with a constant diffusion coefficient. The lack of obvious diffusion pattern suggests that if fluids do play role, the migration path may be complex or indirect. For instance, near-lithostatic pore pressures along patches of active fault zones can enable faults to fail aseismically in slow earthquakes (Liu & Rice, 2009). We observe sporadic fast migration periods that could be associated with slow-slip propagation (Figure S9 in Supporting Information S1).

In summary, our results indicate that the spatiotemporal seismicity distribution during the first three sequences is modulated by the ~250-day slow-slip transient that originated in the northern Armutlu Peninsula on 20 December

2018. The temporal correlation between *b*-value variations and geodetic data indicates that aseismic slip may influence the seismic hazard of target faults. It is not yet well established if slow-slip transients can also modify the frequency-magnitude distribution of earthquakes on nearby faults. If so, it could affect the locked or creeping status of individual fault segments along the Marmara seismic gap (Bohnhoff et al., 2013) and subsequently alter local seismic hazard.

We note that the seismicity analyzed here (25 January 2019 to 7 February 2020) is part of a period of increased seismicity that started at the end of November 2018 and includes a M_w 4.1 and a M_w 4.5 earthquake on 30 November 2018 and 20 December 2018, respectively. The seismicity in the ∼1-month after the M_w 4.5 earthquake deviated from an Omori law decay, suggesting that it does not represent an aftershock sequence (Martínez-Garzón et al., 2021). We note, however, that the interpretation of aseismic and seismic slip interaction on neighboring fault patches is independent of any inferred aftershock sequence that may or may not have been ongoing.

5. Conclusions

We generate an enhanced 1-year microseismicity catalog from a dense local seismic network providing unprecedented resolution in the northern Armutlu Peninsula. We use it to analyze the spatiotemporal seismicity distribution with the goal of exploring the mechanisms driving the local seismic activity and principal deformation mechanisms in the study area. Synthesizing the catalog analysis with available strainmeter data leads to the following findings:

- The occurrence of four spatially and temporally distinct week-long sequences within a narrow ∼60 km^2 area (Esenköy Seismic Zone).
- Seismicity is mostly driven by both aseismic deformation and earthquake-earthquake interactions; the relative dominance of mechanisms varies in time and space over the span of the ∼1 year study period.
- We provide one of the first direct observations of a correlation between a slow-slip transient and seismic *b*-value that highlight the influence of aseismic deformation on seismic slip, as well as the impact of aseismic deformation on local seismic hazard.

Data Availability Statement

Figures were created using the Global Mapping Tool (Wessel et al., 2013) and Matplotlib (Hunter, 2007). Waveform data processing was performed with Obspy v1.1 (Beyreuther et al., 2010). The absolute location and relocated catalogs are available from Bocchini et al. (2022). The relocated catalog used to build template events is available from Martínez-Garzón, Durand, et al. (2022).

Acknowledgments
We thank T. Fischer for proving the code to calculate effective stress drop values, D. Becker for useful discussions on *b*-value and M_c calculations, and C. Chamberlain for help with EQcorrscan. G.M.B. was partially supported through the VW momentum grant awarded to R.M.H.. P.M.G. acknowledges funding from the Helmholtz Association in the frame of the Young Investigators Group VH-NG-1232 (SAIDAN). Seismic instruments of the SMARTnet network were provided by Geophysical Instrument Pool Potsdam (GIPP) of the GFZ, Grant Nos. GIPP201819 and GIPP201921. The authors are grateful to the Editor German A. Prieto and two anonymous reviewers for their constructive comments that helped to improve the initial manuscript. Open Access funding enabled and organized by Projekt DEAL.

References

Armijo, R., Meyer, B., Navarro, S., King, G., & Barka, A. (2002). Asymmetric slip partitioning in the Sea of Marmara pull-apart: A clue to propagation processes of the north Anatolian Fault? *Terra Nova*, *14*(2), 80–86. https://doi.org/10.1046/j.1365-3121.2002.00397.x

Aslan, G., Lasserre, C., Cakir, Z., Ergintav, S., Özarpaci, S., Dogan, U., et al. (2019). Shallow creep along the 1999 Izmit earthquake rupture (Turkey) from GPS and high temporal resolution interferometric synthetic aperture radar data (2011–2017). *Journal of Geophysical Research: Solid Earth*, *124*(2), 2218–2236. https://doi.org/10.1029/2018JB017022

Bachmann, C. E., Wiemer, S., Goertz-Allmann, B. P., & Woessner, J. (2012). Influence of pore-pressure on the event-size distribution of induced earthquakes. *Geophysical Research Letters*, *39*(9), 9302. https://doi.org/10.1029/2012GL051480

Bachura, M., Fischer, T., Doubravová, J., & Horálek, J. (2021). From earthquake swarm to a main shock–aftershocks: The 2018 activity in west Bohemia/Vogtland. *Geophysical Journal International*, *224*(3), 1835–1848. https://doi.org/10.1093/GJI/GGAA523

Barka, A., Akyüz, H. S., Altunel, E., Sunal, G., Çakir, Z., Dikbas, A., et al. (2002). The surface rupture and slip distribution of the 17 August 1999 İzmit earthquake (M 7.4), North Anatolian fault. *Bulletin of the Seismological Society of America*, *92*(1), 43–60. https://doi.org/10.1785/0120000841

Beyreuther, M., Barsch, R., Krischer, L., Megies, T., Behr, Y., & Wassermann, J. (2010). ObsPy: A Python toolbox for seismology. *Seismological Research Letters*, *81*(3), 530–533. https://doi.org/10.1785/GSSRL.81.3.530

Bocchini, G. M., Martínez-Garzón, P., Verdecchia, A., Harrington, R., Bohnhoff, M., Turkmen, T., & Nurlu, M. (2022). Enhanced seismicity catalog for the northern Armutlu Peninsula (northwestern Turkey). [Dataset]. GFZ Data Services. https://doi.org/10.5880/GFZ.4.2.2022.003

Bohnhoff, M., Bulut, F., Dresen, G., Malin, P. E., Eken, T., & Aktar, M. (2013). An earthquake gap south of Istanbul. *Nature Communications*, *4*(1), 1–6. https://doi.org/10.1038/ncomms2999

Bulut, F., Bohnhoff, M., Ellsworth, W. L., Aktar, M., & Dresen, G. (2009). Microseismicity at the north Anatolian Fault in the Sea of Marmara offshore Istanbul, NW Turkey. *Journal of Geophysical Research*, *114*(B9), 9302. https://doi.org/10.1029/2008JB006244

Cappa, F., Scuderi, M. M., Collettini, C., Guglielmi, Y., & Avouac, J. P. (2019). Stabilization of fault slip by fluid injection in the laboratory and in situ. *Science Advances*, *5*(3). https://doi.org/10.1126/sciadv.aau4065

Chamberlain, C. J., Hopp, C. J., Boese, C. M., Warren-Smith, E., Chambers, D., Chu, S. X., et al. (2018). EQcorrscan: Repeating and near-repeating earthquake detection and analysis in Python. *Seismological Research Letters*, *89*(1), 173–181. https://doi.org/10.1785/0220170151

Cruz-Atienza, V. M., Tago, J., Villafuerte, C., Wei, M., Garza-Girón, R., Dominguez, L. A., et al. (2021). Short-term interaction between silent and devastating earthquakes in Mexico. *Nature Communications*, *12*(1), 1–14. https://doi.org/10.1038/s41467-021-22326-6

De Barros, L., Cappa, F., Deschamps, A., & Dublanchet, P. (2020). Imbricated aseismic slip and fluid diffusion drive a seismic swarm in the Corinth Gulf, Greece. *Geophysical Research Letters*, *47*(9), e2020GL087142. https://doi.org/10.1029/2020GL087142

Disaster and Emergency Management Authority, AFAD. (2022). Turkish national seismic network [Data set]. Department of Earthquake, Disaster and Emergency Management Authority. https://doi.org/10.7914/SN/TU

Durand, V., Gualandi, A., Ergintav, S., Kwiatek, G., Haghshenas, M., Motagh, M., et al. (2022). Deciphering aseismic deformation along submarine fault branches below the eastern Sea of Marmara (Turkey): Insights from seismicity, strainmeter, and GNSS data. *Earth and Planetary Science Letters*, *594*, 117702. https://doi.org/10.1016/j.epsl.2022.117702

Eisenlohr, T. (1997). The thermal springs of the Armutlu Peninsula (NW Turkey) and their relationship to geology and tectonic. In C. Schindler & M. Pfister (Eds.), *Active tectonics of northwestern Anatolia—The MARMARA Poly-Project* (pp. 197–228). ETH. Retrieved from https://www.google.com/books?hl=it%26lr=%26id=0Iorly33iDsC%26oi=fnd%26pg=PA197%26dq=Eisenlohr+1997+armutlu%26ots=kmz-51TBbX-%26sig=YGrJRA829g0c-GSV1QRqoZgdids

Fischer, T., & Hainzl, S. (2017). Effective stress drop of earthquake clusters effective stress drop of earthquake clusters. *Bulletin of the Seismological Society of America*, *107*(5), 2247–2257. https://doi.org/10.1785/0120170035

Goebel, T. H. W., Becker, T. W., Schorlemmer, D., Stanchits, S., Sammis, C., Rybacki, E., & Dresen, G. (2012). Identifying fault heterogeneity through mapping spatial anomalies in acoustic emission statistics. *Journal of Geophysical Research*, *117*(B3), 3310. https://doi.org/10.1029/2011JB008763

Goebel, T. H. W., Kwiatek, G., Becker, T. W., Brodsky, E. E., & Dresen, G. (2017). What allows seismic events to grow big? Insights from *b*-value and fault roughness analysis in laboratory stick-slip experiments. *Geology*, *45*(9), 815–818. https://doi.org/10.1130/G39147.1

Hainzl, S. (2016). Rate-dependent incompleteness of earthquake catalogs. *Seismological Research Letters*, *87*(2A), 337–344. https://doi.org/10.1785/0220150211

Hainzl, S., & Fischer, T. (2002). Indications for a successively triggered rupture growth underlying the 2000 earthquake swarm in Vogtland/NW Bohemia. *Journal of Geophysical Research*, *107*(B12), ESE 5-1-ESE 5-9. https://doi.org/10.1029/2002JB001865

Hainzl, S., & Ogata, Y. (2005). Detecting fluid signals in seismicity data through statistical earthquake modeling. *Journal of Geophysical Research*, *110*(5), 1–10. https://doi.org/10.1029/2004JB003247

Hainzl, S., Fischer, T., & Dahm, T. (2012). Seismicity-based estimation of the driving fluid pressure in the case of swarm activity in Western Bohemia. *Geophysical Journal International*, *191*(1), 271–281. https://doi.org/10.1111/j.1365-246X.2012.05610.x

Hawthorne, J. C., Simons, M., & Ampuero, J.-P. (2016). Estimates of aseismic slip associated with small earthquakes near San Juan Bautista, CA. *Journal of Geophysical Research: Solid Earth*, *121*(11), 8254–8275. https://doi.org/10.1002/2016JB013120

Hunter, J. D. (2007). Matplotlib: A 2D graphics environment. *Computing in Science & Engineering*, *9*(3), 90–95. https://doi.org/10.1109/MCSE.2007.55

Kandilli Observatory and Earthquake Research Institute, Boğaziçi University, KOERI. (1971). *Bogazici University Kandilli observatory and earthquake Research Institute. International Federation of digital seismograph networks*. Dataset/Seismic Network. https://doi.org/10.7914/SN/KO

King, G. C. P., Stein, R. S., & Lin, J. (1994). Static stress changes and the triggering of earthquakes. *Bulletin of the Seismological Society of America*, *84*(3), 935–953.

Kinscher, J., Krüger, F., Woith, H., Lühr, B. G., Hintersberger, E., Irmak, T. S., & Baris, S. (2013). Seismotectonics of the Armutlu Peninsula (Marmara Sea, NW Turkey) from geological field observation and regional moment tensor inversion. *Tectonophysics*, *608*, 980–995. https://doi.org/10.1016/J.TECTO.2013.07.016

Koulali, A., McClusky, S., Wallace, L., Allgeyer, S., Tregoning, P., D'Anastasio, E., & Benavente, R. (2017). Slow slip events and the 2016 Te Araroa Mw 7.1 earthquake interaction: Northern Hikurangi subduction, New Zealand. *Geophysical Research Letters*, *44*(16), 8336–8344. https://doi.org/10.1002/2017GL074776

Langenbruch, C., Dinske, C., & Shapiro, S. A. (2011). Inter event times of fluid induced earthquakes suggest their poisson nature. *Geophysical Research Letters*, *38*(21), L21302. https://doi.org/10.1029/2011GL049474

Liu, Y., & Rice, J. R. (2009). Slow slip predictions based on granite and gabbro friction data compared to GPS measurements in northern Cascadia. *Journal of Geophysical Research*, *114*(B9), 9407. https://doi.org/10.1029/2008JB006142

Lohman, R. B., & McGuire, J. J. (2007). Earthquake swarms driven by aseismic creep in the Salton Trough, California. *Journal of Geophysical Research*, *112*(B4), B04405. https://doi.org/10.1029/2006JB004596

Lomax, A., Virieux, J., Volant, P., & Berge-Thierry, C. (2000). Probabilistic earthquake location in 3D and layered models. In C. H. Thurber & N. Rabinowitz (Eds.), *Advances in seismic event location* (pp. 101–134). Kluwer, Springer, https://doi.org/10.1007/978-94-015-9536-0_5

Madariaga, R., & Ruiz, S. (2016). Earthquake dynamics on circular faults: A review 1970–2015. *Journal of Seismology*, *20*(4), 1235–1252. https://doi.org/10.1007/S10950-016-9590-8

Martínez-Garzón, P., Ben-Zion, Y., Zaliapin, I., & Bohnhoff, M. (2019). Seismic clustering in the Sea of Marmara: Implications for monitoring earthquake processes. *Tectonophysics*, *768*, 228176. https://doi.org/10.1016/J.TECTO.2019.228176

Martínez-Garzón, P., Bohnhoff, M., Mencin, D., Kwiatek, G., Dresen, G., Hodgkinson, K., et al. (2019). Slow strain release along the eastern Marmara region offshore Istanbul in conjunction with enhanced local seismic moment release. *Earth and Planetary Science Letters*, *510*, 209–218. https://doi.org/10.1016/j.epsl.2019.01.001

Martínez-Garzón, P., Bohnhoff, M., Turkmen, T., & Nurlu, M. (2022). SMARTnet: Seismic Monitoring of the Armutlu Fault Zone [Dataset]. GFZ Data Services. Other/Seismic Network. https://doi.org/10.14470/4C7564613852

Martínez-Garzón, P., Durand, V., Bentz, S., Kwiatek, G., Dresen, G., Turkmen, T., et al. (2021). Near-fault monitoring reveals combined seismic and slow activation of a fault branch within the Istanbul–Marmara seismic gap in northwest Turkey. *Seismological Research Letters*, *92*(6), 3743–3756. https://doi.org/10.1785/0220210047

Martínez-Garzón, P., Durand, V., Kwiatek, G., Bohnhoff, M., Georg, D., Turkmen, T., & Nurlu, M. (2022). Seismicity catalog for the Armutlu Peninsula from 2019 derived using the SMARTnet temporary seismic network. V. 1 [Dataset]. GFZ Data Services. https://doi.org/10.5880/GFZ.4.2.2021.004

Martínez-Garzón, P., Zaliapin, I., Ben-Zion, Y., Kwiatek, G., & Bohnhoff, M. (2018). Comparative study of earthquake clustering in relation to hydraulic activities at geothermal fields in California. *Journal of Geophysical Research: Solid Earth*, *123*(5), 4041–4062. https://doi.org/10.1029/2017JB014972

Matsuzawa, T., Uchida, N., Igarashi, T., Okada, T., & Hasegawa, A. (2004). Repeating earthquakes and quasi-static slip on the plate boundary east off northern Honshu, Japan. *Earth Planets and Space*, *56*(8), 803–811. https://doi.org/10.1186/BF03353087/METRICS

McGuire, J. J., Boettcher, M. S., & Jordan, T. H. (2005). Foreshock sequences and short-term earthquake predictability on East Pacific Rise transform faults. *Nature*, *434*(7032), 457–461. https://doi.org/10.1038/nature03377

Mouslopoulou, V., Bocchini, G. M., Cesca, S., Saltogianni, V., Bedford, J., Petersen, G., et al. (2020). Earthquake swarms, slow slip and fault interactions at the Western-end of the Hellenic subduction system precede the Mw 6.9 Zakynthos earthquake, Greece. *Geochemistry, Geophysics, Geosystems*, *21*(12), e2020GC009243. https://doi.org/10.1029/2020GC009243

Obara, K., & Kato, A. (2016). Connecting slow earthquakes to huge earthquakes. *Science*, *353*(6296), 253–257. https://doi.org/10.1126/science.aaf1512

Parsons, T. (2004). Recalculated probability of M ≥ 7 earthquakes beneath the Sea of Marmara, Turkey. *Journal of Geophysical Research*, *109*(B5), 5304. https://doi.org/10.1029/2003JB002667

Petersen, G. M., Niemz, P., Cesca, S., Mouslopoulou, V., & Bocchini, G. M. (2021). Clusty, the waveform-based network similarity clustering toolbox: Concept and application to image complex faulting offshore Zakynthos (Greece). *Geophysical Journal International*, *224*(3), 2044–2059. https://doi.org/10.1093/GJI/GGAA568

Ross, Z. E., Cochran, E. S., Trugman, D. T., & Smith, J. D. (2020). 3D fault architecture controls the dynamism of earthquake swarms. *Science*, *368*(6497), 1357–1361. https://doi.org/10.1126/science.abb0779

Scholz, C. H. (1968). The frequency-magnitude relation of microfracturing in rock and its relation to earthquakes. *Bulletin of the Seismological Society of America*, *58*(1), 399–415. https://doi.org/10.1785/BSSA0580010399

Scholz, C. H. (2015). On the stress dependence of the earthquake *b* value. *Geophysical Research Letters*, *42*(5), 1399–1402. https://doi.org/10.1002/2014GL062863

Schorlemmer, D., Wiemer, S., & Wyss, M. (2005). Variations in earthquake-size distribution across different stress regimes. *Nature*, *437*(7058), 539–542. https://doi.org/10.1038/nature04094

Tormann, T., Wiemer, S., Metzger, S., Michael, A., & Hardebeck, J. L. (2013). Size distribution of Parkfield's microearthquakes reflects changes in surface creep rate. *Geophysical Journal International*, *193*(3), 1474–1478. https://doi.org/10.1093/GJI/GGT093

Tormann, T., Wiemer, S., & Mignan, A. (2014). Systematic survey of high-resolution b value imaging along Californian faults: Inference on asperities. *Journal of Geophysical Research: Solid Earth*, *119*(3), 2029–2054. https://doi.org/10.1002/2013JB010867

Uchida, N., & Bürgmann, R. (2019). Repeating earthquakes. *Repeating Earthquakes*, *47*(1), 305–332. https://doi.org/10.1146/ANNUREV-EARTH-053018-060119

Uchida, N., Iinuma, T., Nadeau, R. M., Bürgmann, R., & Hino, R. (2016). Periodic slow slip triggers megathrust zone earthquakes in northeastern Japan. *Science*, *351*(6272), 488–492. https://doi.org/10.1126/science.aad3108

Utsu, T. (1965). A method for determining the value of "b" in a formula log n = a-bM showing the magnitude-frequency relation for earthquakes. *Geophysical Bulletin of Hokkaido University*, *13*, 99–103. Retrieved from https://ci.nii.ac.jp/naid/10009630720

Verdecchia, A., Cochran, E. S., & Harrington, R. M. (2021). Fluid-earthquake and earthquake-earthquake interactions in southern Kansas, USA. *Journal of Geophysical Research: Solid Earth*, *126*(3), e2020JB020384. https://doi.org/10.1029/2020JB020384

Waldhauser, F. (2001). HypoDD-A program to compute double-difference hypocenter locations (version 1.). Open-file report. Retrieved from http://pubs.er.usgs.gov/publication/ofr01113

Warren-Smith, E., Fry, B., Wallace, L., Chon, E., Henrys, S., Sheehan, A., et al. (2019). Episodic stress and fluid pressure cycling in subducting oceanic crust during slow slip. *Nature Geoscience*, *12*(6), 475–481. https://doi.org/10.1038/s41561-019-0367-x

Wessel, P., Smith, W. H. F., Scharroo, R., Luis, J., & Wobbe, F. (2013). Generic mapping tools: Improved version released. *Eos*, *94*(45), 409–410. https://doi.org/10.1002/2013EO450001

Wiemer, S., & Wyss, M. (2000). Minimum magnitude of completeness in earthquake catalogs: Examples from Alaska, the Western United States, and Japan. *Bulletin of the Seismological Society of America*, *90*(4), 859–869. https://doi.org/10.1785/0119990114

Yoshida, K., Saito, T., Urata, Y., Asano, Y., & Hasegawa, A. (2017). Temporal changes in stress drop, frictional strength, and earthquake size distribution in the 2011 Yamagata-fukushima, NE Japan, earthquake swarm, caused by fluid migration. *Journal of Geophysical Research: Solid Earth*, *122*(12), 10379–10397. https://doi.org/10.1002/2017JB014334

Zaliapin, I., & Ben-Zion, Y. (2013a). Earthquake clusters in southern California I: Identification and stability. *Journal of Geophysical Research: Solid Earth*, *118*(6), 2847–2864. https://doi.org/10.1002/JGRB.50179

Zaliapin, I., & Ben-Zion, Y. (2013b). Earthquake clusters in southern California II: Classification and relation to physical properties of the crust. *Journal of Geophysical Research: Solid Earth*, *118*(6), 2865–2877. https://doi.org/10.1002/JGRB.50178

Zaliapin, I., & Ben-Zion, Y. (2016). Discriminating characteristics of tectonic and human-induced seismicity. *Bulletin of the Seismological Society of America*, *106*(3), 846–859. https://doi.org/10.1785/0120150211

Zaliapin, I., Gabrielov, A., Keilis-Borok, V., & Wong, H. (2008). Clustering analysis of seismicity and aftershock identification. *Physical Review Letters*, *101*(1), 018501. https://doi.org/10.1103/PhysRevLett.101.018501

References From the Supporting Information

Bohnhoff, M., Dresen, G., Ceken, U., Kadirioglu, F. T., Kartal, R. F., Kilic, T., et al. (2017). GONAF—the borehole geophysical observatory at the north Anatolian Fault in the eastern Sea of Marmara. *Scientific Drilling*, *22*, 19–28. https://doi.org/10.5194/SD-22-19-2017

Ester, M., Kriegel, H.-P., Sander, J., & Xu, X. (1996). A density-based algorithm for discovering clusters in large spatial databases with noise. *KDD*, *96*(34), 226–231. Retrieved from www.aaai.org

Maurer, H., & Deichmann, N. (1995). Microearthquake cluster detection based on waveform similarities, with an application to the Western Swiss Alps. *Geophysical Journal International*, *123*(2), 588–600. https://doi.org/10.1111/J.1365-246X.1995.TB06873.X

Schaff, D. P., & Richards, P. G. (2014). Improvements in magnitude precision, using the statistics of relative amplitudes measured by cross correlation. *Geophysical Journal International*, *197*(1), 335–350. https://doi.org/10.1093/GJI/GGT433

Wiemer, S. (2001). A software package to analyze seismicity: ZMAP. *Seismological Research Letters*, *72*(3), 373–382. https://doi.org/10.1785/gssrl.72.3.373